Why is only type 1 electrocardiogram diagnostic of Brugada Syndrome? Mechanistic insights from computer modeling

Zhaoyang Zhang, PhD[1], **Peng-Sheng Chen, MD**[2], **James N. Weiss, MD**[3], **Zhilin Qu, PhD**[3,4]

[1]Department of physics, School of Physical Science and Technology, Ningbo University, Ningbo, Zhejiang 315211, China

[2]Department of Cardiology, Cedars Sinai Medical Center, Los Aneles, CA 90048, USA

[3]Department of Medicine, David Geffen School of Medicine, University of California, Los Angeles, California 90095, USA

[4]Department of Computational Medicine, David Geffen School of Medicine, University of California, Los Angeles, California 90095, USA

Abstract

Background.—Three types of characteristic ST-segment elevation are associated with Brugada syndrome (BrS) but only type 1 is diagnostic. Why only type 1 electrocardiogram (ECG) is diagnostic remains unanswered.

Methods.—Computer simulations were carried out in single cells, one-dimensional cables, and two-dimensional tissues to investigate the effects of the peak and late components of the transient outward potassium current (I_{to}), sodium current (I_{Na}), and L-type calcium current ($I_{Ca,L}$) as well as other potassium currents on the genesis of ECG morphologies and phase 2 reentry (P2R).

Results.—Although a sufficiently large peak I_{to} was required to result in the type 1 ECG pattern and P2R, increasing the late component of I_{to} converted type 1 ECG to type 2 ECG and suppressed P2R. Increasing the peak I_{to} promoted spiral wave breakup, potentiating the transition from tachycardia to fibrillation, but increasing the late I_{to} prevented spiral wave breakup by flattening the action potential duration restitution and preventing P2R. A sufficiently large $I_{Ca,L}$ conductance was needed for P2R to occur, but once above the critical conductance, blocking $I_{Ca,L}$ promoted P2R. However, selectively blocking the window and late components of $I_{Ca,L}$ suppressed P2R, countering the effect of the late I_{to}. Blocking either the peak or late components of I_{Na} promoted P2R, with the late I_{Na} blockade having the larger effect. As expected, increasing other potassium currents potentiated P2R, with I_{K-ATP} exhibiting a larger effect than I_{Kr} and I_{Ks}.

Correspondence to: Zhilin Qu, PhD, Department of Medicine, Division of Cardiology, David Geffen School of Medicine at UCLA, A2-237 CHS, 650 Charles E. Young Drive South, Los Angeles, CA 90095, zqu@mednet.ucla.edu.

Disclosure: None

Supplemental Materials
Supplemental Methods
Supplemental Table I
Supplemental Figures I–X
Supplemental Movies I–IV

Conclusions.—The peak I_{to} promotes type 1 ECG and P2R, whereas the late I_{to} converts type 1 ECG to type 2 ECG and suppresses P2R. Blocking the peak $I_{Ca,L}$ and either the peak or the late I_{Na} promotes P2R whereas blocking the window and late $I_{Ca,L}$ suppresses P2R. These results provide important insights into the mechanisms of arrhythmogenesis and potential therapeutic targets for treatment of BrS.

Graphical Abstract
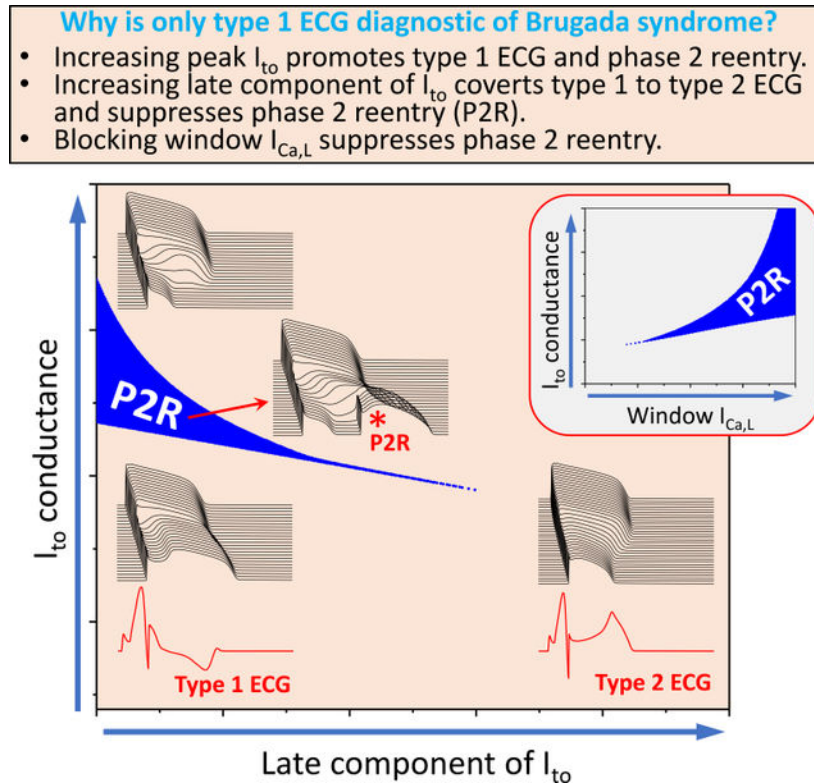
Keywords

Brugada syndrome; type 1 ECG; phase 2 reentry; late current; computer simulation

Introduction

Brugada syndrome (BrS) is an inherited heart disease characterized by J-point and ST-segment elevation in surface ECG and associated with a high risk of sudden cardiac death [1–4]. As described in current consensus statements [5–7], there are three types of characteristic ECGs associated with BrS (see Fig.I in Data Supplement). Type 1 is characterized by coved ST-segment elevation >2 mm in leads V1-V3 with a negative T-wave, type 2 by a saddleback ST-segment elevation >2 mm, and type 3 with either coved or saddleback ST-segment ST elevation <1 mm. In all three types of ECGs, the J-point is elevated. However, only type 1 is diagnostic of BrS [5–7]. Patients exhibiting type 2 or type 3 ECGs can sometimes be converted to type 1 by provocative drugs such Na^+ channel blockers, but still have very low risk of arrhythmias [7, 8].

The cellular mechanisms of coved and saddleback ECGs have been linked to the spike-and-dome action potential (AP) morphology caused by the transient outward K^+ current (I_{to}) by Antzelevitch and coworkers [9], who also showed that the spike-and-dome AP morphology promotes phase 2 reentry (P2R) initiating ventricular fibrillation [10–12]. However, why only type 1 ECGs are diagnostic of BrS and confer a high risk of sudden cardiac death remains unanswered. In this study, we used computer models to investigate the mechanisms underlying the three characteristic ECG morphologies and their links to arrhythmogenesis. We carried out simulations in single cells, one-dimensional (1D) cables, and two-dimensional (2D) tissues to investigate the effects of the peak and late components of I_{to}, the L-type calcium current ($I_{Ca,L}$) and the sodium current (I_{Na}). We also investigated the effects of other K^+ currents, i.e., the rapid (I_{Kr}) and slow (I_{Ks}) components of the delayed rectifier K^+ current, and the ATP-sensitive K^+ current ($I_{K\text{-}ATP}$). We show that while a sufficiently large peak I_{to} is required to initiate phase 2 reentry (P2R), increasing the late component of I_{to} converts type 1 ECG to type 2 ECG and suppresses P2R. Increasing the peak I_{to} promotes spiral wave breakup, but increasing the late I_{to} prevents spiral wave breakup by flattening the AP duration (APD) restitution and preventing focal excitations. For $I_{Ca,L}$, a sufficiently large peak conductance is required for P2R, but above a critical conductance, further increases in $I_{Ca,L}$ suppress P2R. Moreover, increasing the window and late $I_{Ca,L}$ promotes P2R by countering the P2R-suppressing effect of the late I_{to}. For I_{Na}, blocking either the peak or the late component promotes P2R, with the late I_{Na} blockade exhibiting the larger effect. Increasing other K^+ currents, such as I_{Ks}, I_{Kr} or $I_{K\text{-}ATP}$, can promote P2R, with $I_{K\text{-}ATP}$ exhibiting the largest effect. Men are more susceptible to P2R, mainly because men have a larger I_{to} and a smaller $I_{Ca,L}$ than women. For the same reason, P2R is more likely to occur at nighttime than daytime. The implications for arrhythmogenesis and therapies of BrS are discussed.

Methods

The data that support the findings of this study are available from the corresponding author upon reasonable request. No institutional review board approval was necessary since only simulations were performed.

1D cable and 2D tissue model.

We carried out single cell, 1D cable, and 2D tissue simulations. For the 1D cable model, the governing equation for voltage (V) is:

$$\frac{\partial V}{\partial t} = -\frac{I_{ion} + I_{sti}}{C_m} + D_x \frac{\partial^2 V}{\partial x^2} \tag{1}$$

where C_m is the capacitance and I_{ion} is the total ionic current density described by the 1994 Luo and Rudy model [13]. I_{sti} is the stimulus current density of a 0.5 ms pulse with a −80 $\mu A/cm^2$. D_x is the diffusion constant representing the gap junction coupling strength.

The governing equation for voltage in the 2D tissue model is:

$$\frac{\partial V}{\partial t} = -\frac{I_{ion} + I_{sti}}{C_m} + D_x\frac{\partial^2 V}{\partial x^2} + D_y\frac{\partial^2 V}{\partial y^2} \tag{2}$$

We also performed 1D cable and 2D tissue simulations using the 2004 ten Tusscher et al human ventricular AP model [14] and the results are shown in Figs.V–X and Movies II–IV in Data Supplement. The parameter settings for heterogeneities, calculation of pseudo-ECG, and the numerical methods are also presented as supplemental methods in Data Supplement. Unless stated specifically, the parameters were the same as in the original cell models.

I_{to} model.

For either the 1994 Luo and Rudy model or the 2004 ten Tusscher et al model, we used (or substituted the I_{to} in the ten Tusscher et al model with) the I_{to} formulation by Dumaine et al [15]:

$$I_{to} = G_{to}z^3 y e^{\frac{V}{100}}\left(V - E_K\right) \tag{3}$$

where G_{to} is the maximum conductance, z is the activation gating variable, and y is the inactivation gating variable. To vary the late component of I_{to}, we altered the steady-state inactivation as

$$y_{\infty, new} = \gamma + (1 - \gamma)y_{\infty} \tag{4}$$

where γ controls the strength of the late I_{to} and increasing γ increases the late component.

Results

Late I_{to} coverts type 1 ECG to type 2 ECG and prevents P2R

We first carried out 2D tissue simulations to demonstrate the effects of late I_{to} on ECG morphology and the occurrence of P2R. We altered the late I_{to} in the model by changing γ as described in Eq.4. Fig.1A shows the time-space plots of voltage and the corresponding pseudo-ECGs for different maximum I_{to} conductance (G_{to}) for $\gamma = 0$. When $G_{to}=0$, the T-wave was upright since the APD was shorter in the epicardium. As G_{to} was increased, the J-point and the ST-segment became elevated, and the T-wave amplitude became smaller and then negative. When G_{to} was large still, the ST-segment then became coved (type 1) and spontaneous PVCs began to occur. As G_{to} was increased even further, the APD shortened on the epicardial side and the ST-segment became highly elevated, but spontaneous PVCs disappeared. The coved ECGs were also promoted by blocking I_{Na} or $I_{Ca,L}$ when G_{to} was large enough (see Fig.II in Data Supplement). For $\gamma = 0.1$ (Fig.1B), both the J-point and ST-segment become elevated with a saddleback ST-segment (type 2) as G_{to} was increased, but no PVCs occurred for any G_{to} values.

In simulated 2D tissue with an endo-epi gradient in I_{to} density, PVCs occurred, but reentry was never observed. However, when a longitudinal gradient in I_{to} density was also introduced, spontaneous PVCs began to initiate reentry. Fig.1C shows voltage snapshots at

different time points illustrating the spontaneous formation of reentry in the 2D tissue model with both transmural and longitudinal heterogeneities (see Movie I in Data Supplement for the entire episode). Note that after the first episode of P2R, repolarization heterogeneities became very dynamic, resulting in additional P2R episodes at different locations in the tissue. Depending on the tissue size and degree of heterogeneity, P2R could manifest as a single PVC or induce non-sustained and sustained arrhythmias.

To provide a systematic analysis of the effects I_{to} on P2R, we carried out simulations in a 1D cable in which all other ionic currents were uniform except I_{to}. G_{to} in one half (the "endocardial" side) of the cable was zero and the other half (the "epicardial" side) was non-zero, as illustrated in the inset of Fig.2D. The cable was paced from the "endocardial" side. In the 1D cable, only PVCs were observed, which, for simplicity, we also call P2Rs. Fig.2A shows the P2R region versus G_{to} and γ from the 1D cable simulations obtained by scanning G_{to} and γ with small increments. At $\gamma = 0$, P2R occurred for G_{to} between 1.59 and 1.85 mS/cm^2 (see the middle panel in Fig.2B for an example of time-space plot of voltage for P2R). When G_{to} was smaller than 1.59 mS/cm^2, the spike-and-dome AP morphology occurred in the epicardial side of the cable (see the lower panel in Fig.2B) with a later repolarization. When G_{to} was larger than 1.85 mS/cm^2, the AP became a spike on the epicardial side with very early repolarization (see the upper panel in Fig.2B). In this case, the tissue was very heterogeneous. Although the G_{to} threshold for P2R (the boundary between "Spike & Dome" and "P2R") decreased as γ increased, the P2R region shrank quickly, and no P2R occurred when $\gamma > 0.06$. This agrees with the observation in Fig.1 that increasing the late I_{to} converts type 1 ECG to type 2 ECG and suppresses P2R.

We also investigated the effects of window I_{to} and inactivation time constant on P2R. Fig.2C shows the P2R region versus G_{to} and the voltage shift (V_{shift}) of the steady-state inactivation curve (y_∞). Increasing the window I_{to} (shifting the curve rightward, $V_{shift} > 0$) shrank the G_{to} range for P2R. However, this also caused P2R to occur at a lower G_{to}. Slowing inactivation suppressed the G_{to} range for P2R but also lowered the G_{to} threshold. Note that increasing the window I_{to} or slowing I_{to} inactivation exhibited a much larger effect on lowering the G_{to} threshold for P2R than increasing γ. This is because shifting y_∞ or slowing inactivation increased the late component of I_{to}, which tended to suppress P2R, but also increased the amplitude of I_{to}, which lowered the G_{to} threshold for P2R. Therefore, it is unclear if a strategy of altering window I_{to} or its inactivation time constant would promote or suppress P2R.

In Fig.2, the simulations were performed for a fixed initial condition with a single pacing beat. To investigate how continuous pacing and late I_{to} affect P2R, we paced the cable with two other pacing protocols: periodic pacing and random pacing (Fig.3). Fig.3A shows the P2R region and percent of the beats exhibiting PVCs versus G_{to} and pacing cycle length (PCL) for $\gamma = 0$, $\gamma = 0.02$, and $\gamma = 0.05$. The P2R region (G_{to} range) decreased as PCL was increased or as γ was increased. Moreover, the percentage of the beats exhibiting PVCs increased with PCL but decreased sharply with γ. Note that although the cable was paced periodically, not all beats exhibited PVCs due to the complex dynamics (see a time-space plot of voltage for an example in Fig.III in Data Supplement). In the simulations in Fig.3A, we only paced 200 beats for each combination of G_{to} and PCL. To obtain more accurate

statistics on PVC rates, we paced 2000 beats for a fixed PCL (1500 ms) and different G_{to} for the three γ values. We calculated the percentage of the beats exhibiting a PVC and plotted it against G_{to} in Fig.3B for the three γ values. For $\gamma = 0$, the highest PVC rate was 60%. When $\gamma = 0.02$, the highest PVC rate was less than 10% and decreased to less than 1% for $\gamma = 0.05$. We did not observe any PVCs for $\gamma > 0.07$ for the 2000 pacing beats. We also used a random pacing protocol in which we randomly picked the PCLs in the interval from 500 ms to 1500 ms, and paced for 2000 beats for each chosen G_{to}. Fig.3C shows the percentage of the beats exhibiting PVCs against G_{to} for the three γ values. The PVC rates became lower but the G_{to} ranges were wider than for the periodic pacing. We did not observe any PVCs when used $\gamma=0.05$ or larger.

Note that although P2R occurred over a wider G_{to} range for the periodic and random pacing protocols (Fig.3) than those for the single-beat pacing (Fig.2A), the likelihood of P2R occurrence decreased sharply with γ in all three pacing protocols, and the threshold γ values for complete suppression of P2R were similar.

Late I_{to} stabilizes spiral wave reentry

In a previous study [16], we showed that I_{to} could destabilize spiral wave reentry, causing spiral wave breakup. Here we show that the late I_{to} stabilizes reentry and can prevent the spiral wave breakup caused by the peak I_{to}. Fig.4A shows voltage snapshots for four G_{to} values with $\gamma = 0$. When G_{to} was small, the spiral wave was stable. When G_{to} was in the intermediate range, spiral wave breakup occurred. When G_{to} was large, the spiral wave became stable again. The mechanisms that I_{to} promotes spiral wave instabilities have been investigated in our previous study [16]. Fig.4B shows voltage snapshots for the same G_{to} values with $\gamma = 0.2$, and the spiral waves were all stable. In Fig.4C, we show the spiral wave cycle length (CL) versus γ for the two G_{to} values (1.5 and 3.2 mS/cm^2) that gave rise to spiral wave breakup in Fig.4A, showing that increasing γ stabilized the spiral wave reentry, i.e., the CL became less variable and finally constant as γ was large enough.

Mechanistic insights from cellular dynamics caused by late I_{to}

To better understand the effects of late I_{to} on the ECG morphology, P2R generation, and reentry stability, we carried out single-cell simulations to investigate the effects of the late I_{to} on APD, APD restitution, and APD dynamics. Fig.5A shows APD versus G_{to} for three γ values. For $\gamma = 0$, as G_{to} was increased from zero, APD increased slowly at first and then rapidly to a maximum before a sudden and discontinuous shortening (an all-or-none response). As γ was increased, the spike-and-dome morphology was attenuated, the APD lengthening was less prominent, and the sudden shortening was attenuated. When γ was large enough, the APD exhibited a continuous and graded response to G_{to}. Figs.5 B and C show APD restitution curves for different G_{to} for $\gamma = 0$ and $\gamma = 0.2$, respectively. For $\gamma = 0$ (Fig.5B), if G_{to} was small, we observed a regular monotonic APD restitution curve. For larger G_{to}, APD first increased with DI but then shortened suddenly and discontinuously at a certain DI, resulting in non-monotonic restitution curves. For $\gamma = 0.2$ (Fig.5C), APD increased with DI, similar to the regular monotonic APD restitution curve but became less steep with larger G_{to}. To show how G_{to} and γ affect the cellular APD dynamics, we paced the cell periodically. Fig.5D is a bifurcation diagram showing APD versus G_{to} for $\gamma = 0$.

APD was regular for either small G_{to} or large G_{to}, but for the intermediate G_{to}, complex APD dynamics, such as alternans, high periodic and non-periodic behaviors occurred (see the example shown in Fig.5E). Increasing γ stabilized the APD dynamics (Fig.5F). I_{to}-promoted complex APD dynamics have been demonstrated previously in experiments and simulations [17–21].

The single-cell simulation results shown in Figs.5A–F provided the following mechanistic insights:

1. When the late I_{to} was small (e.g., the $\gamma = 0$ case in Fig.5A), APD increased with G_{to} but then suddenly shortened due to the sudden loss of the dome. Lengthening APD in the epicardial side resulted in a later repolarization, causing the positive T-wave to become negative and thus giving rise to the coved ST-segment. The sudden shortening of APD resulted in a large repolarization gradient, which together with a prominent spike-and-dome morphology resulted in P2R (see Fig.1A or Fig.2B). When the late I_{to} was large (e.g., the $\gamma = 0.2$ case in Fig.5A), APD decreased as G_{to} was increased, and APD remained shorter on the epicardial side than the endocardial side, which elevated both the ST-segment and the T-wave, resulting in the saddleback ST-segment.

2. In an experimental study, Aiba et al [22] showed different APD restitution properties under control conditions (Fig.5G), BrS with VF (Fig.5H), and BrS with VT (Fig.5I). The APD restitution curve under control conditions was a regular monotonic curve, which corresponded to the curves in the model for small G_{to} (Figs.5 B and C). For the BrS VF case, the APD restitution became a non-monotonic curve, in which APD first increased to a maximum and then decreased quickly as DI was increased. A similar restitution behavior was also observed experimentally in canine ventricular epicardial myocytes [17]. This property agrees well with the APD restitution property in the model for small γ and large G_{to} (see Fig.5B). As shown in our simulations (Fig.4), spiral wave breakup occurred for small γ and large G_{to}. This agrees with the experimental observation that the non-monotonic APD restitution is associated with VF. For the BrS VT case, the APD restitution curve was flattened, which agrees with the APD restitution curves of the model when γ was large (Fig.5C). As shown in our simulations (Fig.4), increasing γ stabilized spiral waves. This agrees with the experimental observation that flatted APD restitution is associated with VT rather than VF. Therefore, our simulations agree with the experimental observations, providing mechanistic links between the late I_{to}, APD restitution, and VT and VF in BrS.

Effects of $I_{Ca,L}$ and I_{Na} on P2R

As shown above, the peak and late I_{to} exhibited opposite effects on the genesis of P2R and reentry stability. Since $I_{Ca,L}$ and I_{Na} also play important roles in arrhythmogenesis in BrS (by adjusting the background conditions upon which I_{to} operates), we investigated whether the different components of these two currents exhibit different effects on the genesis of P2R.

Fig.6 shows the effects of the different $I_{Ca,L}$ components on the genesis of P2R. Fig.6A plots the P2R region versus P_{Ca} and G_{to}. P_{Ca} is the parameter describing the maximum conductance of $I_{Ca,L}$. For P2R to occur, a minimum P_{Ca} was needed. As P_{Ca} was increased, the G_{to} range for P2R increased, but at the same time, the G_{to} threshold for P2R became higher. Therefore, under the right conditions in which P_{Ca} was high, P2R could be promoted by reducing P_{Ca}. Fig.6B shows the P2R region versus γ and P_{Ca}, illustrating that although increasing γ lowered the P_{Ca} threshold (i.e., P2R occurs at a larger P_{Ca}), it quickly suppressed the P_{Ca} range for P2R. Removing the late component of $I_{Ca,L}$ by removing the incomplete steady-state inactivation from the original formulation (see Fig.6F) resulted in a smaller P_{Ca} range of P2R (Fig.6C), indicating that P2R was potentiated by the late $I_{Ca,L}$. Increasing the window $I_{Ca,L}$ (by shifting the steady-state inactivation curve rightward) raised the G_{to} threshold slowly but quickly increased the G_{to} range of P2R (Fig.6D). To show how the window $I_{Ca,L}$ interacts with late I_{to}, we show in Fig.6E the P2R region versus γ and the voltage shift (V_{shift}) of the steady-state inactivation curve, showing that as γ was increased, the V_{shift} range for P2R remained roughly the same. This indicates that the effects of late I_{to} could be countered by the window $I_{Ca,L}$. The effects of late I_{to} could also be countered by the late $I_{Ca,L}$ (see Fig.IV in Data Supplement). This is different from Fig.2A, Figs.6 B and C, in which the P2R regions shrank quickly with γ. The results in Fig.6 show that blocking the peak $I_{Ca,L}$ may promote P2R by bringing the system closer to the threshold, but blocking the window and late $I_{Ca,L}$ can effectively suppress P2R by reducing the size of the P2R region.

Fig.7 illustrates the effects of the peak and late I_{Na} on the genesis of P2R. We added the formulation of late I_{Na} from Hund Rudy[23] into the model. Fig.7A is a plot of the P2R region versus G_{Na} and G_{to}, showing that changing G_{Na} had a small effect on both the G_{to} threshold and the G_{to} range for P2R. For certain G_{to} values (e.g., $G_{to}=1.5$ mS/cm^2), reducing G_{Na} could promote P2R, indicating that blocking I_{Na} potentiates P2R. Fig.7B is a plot of the P2R region versus G_{Na} and P_{Ca}, showing that reducing G_{Na} slightly elevated the P_{Ca} threshold but had little effect on the P_{Ca} range for P2R. Fig.7C plots the P2R region versus the maximum conductance of late I_{Na} (G_{NaL}) and G_{to}, showing that increasing G_{NaL} had a small effect on the G_{to} range for P2R but raised the G_{to} threshold for P2R. Fig.7D plots the P2R region versus γ and G_{NaL}, showing that increasing γ raised the G_{NaL} threshold for P2R slightly, but the G_{NaL} range for P2R shrank quickly. Thus, unlike the window $I_{Ca,L}$, the effects of the late I_{Na} are not countered by the effects of the late I_{to} component but rather by the effects of the peak I_{to} (Fig.7C).

Effects of sex difference and circadian rhythm on P2R

The vast majority of BrS patients are male (91.3%) [24] with arrhythmia risk being higher after midnight [25–28], possibly because current densities differ in male and female hearts and exhibit different responses to sex hormones [29–34] and circadian rhythm [35–37]. To investigate the effects on P2R, we carried out additional 1D cable simulations. We set the female-to-male ratios of the maximum conductance of the ionic currents (See Table I in Data Supplement) based on previous studies[30, 33]. The K$^+$ currents are smaller and $I_{Ca,L}$ is larger in female than in male. Fig.8A shows the P2R regions versus fold change of the maximum conductance of $I_{Ca,L}$ and I_{to} for male (blue) and female (red). The P2R region was much

smaller for female than for male, and started at a lower fold change of $I_{Ca,L}$ and a higher fold change of I_{to}. Therefore, a much larger increase in I_{to} and/or a much larger reduction in $I_{Ca,L}$ is required to produce P2R in females, agreeing with the clinical profile of BrS occurring predominantly in men. Fig.8B plots the P2R regions for male and female versus the fold changes of $I_{Ca,L}$ and I_{Ks}, showing that increasing G_{Ks} exhibited a very small effect on promoting P2R. It has been shown that $I_{Ca,L}$ is reduced during nighttime [35, 36] while I_{to} is increased during nighttime [37] (as indicated by the arrow from sun to moon in Fig.8A). In addition, β-adrenergic activity, which elevates both $I_{Ca,L}$ and I_{Ks}, is higher during daytime than nighttime and thus both $I_{Ca,L}$ and I_{Ks} are smaller during nighttime than daytime (as indicated by the arrow from sun to moon in Fig.8B). Therefore, our simulations indicate that P2R is more likely to occur during nighttime than daytime, agreeing with the clinical observation. Figs.8 C and D show two sets of additional simulations for the effects of I_{Kr} and I_{K-ATP} on P2R. The mathematical model of I_{K-ATP} was taken from Shaw and Rudy [38]. Increasing G_{Kr} or G_{K-ATP} caused P2R to occur at a larger P_{Ca}, indicating that increasing I_{Kr} or I_{K-ATP} promotes P2R. Note that for the three K^+ currents (Figs.8 B–D), I_{K-ATP} exhibits the largest effect on promoting P2R and I_{Ks} the smallest effect, which is more prominent in the ten Tusscher et al human model (see Fig.X in Data Supplement).

Discussion

Three types of characteristic ECGs are associated with BrS, but only type 1 is diagnostic. In this study, we carried out computer simulations to investigate the effects of different components of I_{to}, $I_{Ca,L}$, and I_{Na}, as well as other K^+ currents, on the genesis of P2R and the stability of reentry in BrS. Our major findings are that the late I_{to} component suppresses the spike-and-dome morphology and shortens APD, converting type 1 ECG to type 2 ECG and preventing P2R. The peak I_{to} promotes spiral wave breakup, promoting VF, but the late I_{to} stabilizes reentry, converting VF to VT. Blocking the peak $I_{Ca,L}$ potentiates P2R but blocking the window or the late $I_{Ca,L}$ suppresses P2R. Bocking the peak or the late I_{Na} promotes P2R with the late I_{Na} exhibiting a larger effect. Increasing other K^+ currents, such as I_{Ks}, I_{Kr} or I_{K-ATP}, can promote P2R, with I_{K-ATP} exhibiting the largest effect. Men is more susceptible to P2R, mainly due to that men have a larger I_{to} and a smaller $I_{Ca,L}$ than women. For the same reason, P2R is more likely to occur at nighttime than daytime. We performed the same simulations using the ten Tusscher et al human ventricular AP model [14] and obtained almost the same results (see Figs.V–X in Data Supplement), indicating that the findings are not likely model dependent. The mechanistic insights from our computer simulation results and the implications for arrhythmogenesis and potential therapies for BrS are discussed below.

Ionic mechanisms of ECG morphology and links to P2R

The AP configurations giving rise to coved and saddleback ECG were first proposed by Antzelevitch [9], and our simulations agree with their interpretation. An additional insight from our simulations is the contribution of the late I_{to} component to the ECG characteristics. Combined with the insight from our simulations into the role of late I_{to} in the genesis of P2R, we link the ECG characteristics with the genesis of P2R. More specifically, when I_{to} is large with a small late component, the spike-and-dome AP morphology is prominent and

a coved ST-segment (type 1) occurs (e.g., the case with G_{to}=1.5 in Fig.1A). When I_{to} and its late component are both small, a type 3 ECG occurs (e.g., the cases with G_{to}=0.5 and 1 in Fig.1A). When the late component is large, the AP dome is attenuated and a saddleback ST-segment (type 2) occurs (e.g., the cases with G_{to}=0.5 and 1 in Fig.1B). Since a large I_{to} is needed for P2R, the I_{to} giving rise to type 3 ECG is still far away from the threshold for P2R. For the I_{to} giving rise to type 2 ECG, its late component maybe too strong to allow P2R to occur. Note that when the overall I_{to} is very large with or without the late component, APD becomes very short in the epicardium (the "Spike" regions in Figs. 2, 6, and 7), resulting in a highly elevated ST-segment (e.g., the large G_{to} cases in Figs. 1 A and B). The effects of the late I_{to} can be countered by the window or the late $I_{Ca,L}$.

Roles of late I_{to} on P2R formation and stability

Unlike the traditional mechanisms of reentry formation in which a PVC and a vulnerable heterogeneous tissue substrate may arise from independent processes [39], the PVC and heterogeneous tissue substrate in P2R arise from the same dynamical process. Mechanisms of P2R have been investigated in computer simulation studies [40, 41]. In a recent study [42], we analyzed the dynamical mechanisms of P2R genesis and showed that the occurrence of P2R is determined by two factors: 1) the transition from the spike-and-dome AP morphology to the spike AP morphology in the single cell; and 2) the spatial instability caused by the repolarization heterogeneity in tissue. The former determines the parameter threshold and the later determines the size (or the parameter range) of the P2R region. For example, for $\gamma = 0$, the spike-and-dome to spike transition in the single cell occurs at G_{to}=1.59 mS/cm^2 (Fig.5A) while the G_{to} threshold for P2R in the cable is also 1.59 mS/cm^2 (Fig.2A). Increasing γ reduces the G_{to} for the spike-and-dome to spike transition (Fig.5A), agreeing with increasing γ decreasing the threshold for P2R (Fig.2A). Even for $\gamma = 0$, P2R occurs in a range of G_{to} above the threshold, and when I_{to} is too strong, P2R is suppressed due to suppression of the spatial instability [42]. As shown in Fig.2A, the late I_{to} exhibits a strong effect on suppressing the spatial instability, i.e., the P2R region is reduced quickly as γ increases. In the diagrams shown in Figs.2, 6, and 7, the parameter threshold is the boundary between the "Spike & Dome" and "P2R" and the gray region is the parameter range for P2R. As shown in these figures, different ionic currents or their different components exhibit different effects on the threshold for P2R and the size of the P2R region.

Besides suppressing the genesis of P2R, late I_{to} can also prevent spiral wave breakup. We showed in a previous study [16] that I_{to} could promote spiral wave breakup by steepening the APD restitution curves. Besides the steep APD restitution-induced breakup, we also observed P2Rs resulting from the complex wave dynamics, giving rise to a mixture of spontaneous firings (P2Rs) and spiral wave reentry (see Fig.VII and Movies III and IV in Data Supplement). Since late I_{to} flattens APD restitution and suppresses P2R, it stabilizes spiral wave reentry, preventing the occurrence of VF. This provides an ionic mechanism for the association of VT and VF to the different APD restitution properties observed in the experiments by Aiba et al [22].

The late component of I_{to} can be caused by incomplete inactivation or slow inactivation. As shown in Fig.2D, speeding up inactivation enlarges the region but elevates the G_{to}

threshold for P2R. Therefore, whether a drug that speeds up inactivation is anti- or pro-arrhythmic depends on the relative effects on the peak and the late components. For example, experimental studies showed that acacetin caused a faster inactivation and greatly reduced the amplitude of I_{to} [43], which effectively prevented P2R [44]. On the other hand, the ability of ajmaline and flecainide to promote type 1 ECG and P2R has been attributed to their effects on blocking I_{Na}. However, it is also shown that they may reduce I_{to} by speeding up inactivation [45–47]. Reducing peak I_{to} might oppose their effect on suppressing P2R, but reducing the late component due to fast inactivation might promote type 1 ECG and P2R. Therefore, whether a drug speeding up I_{to} inactivation promotes or suppresses P2R may depend on its differential effects on reducing the peak and the late components of I_{to}.

Implications to arrhythmogenesis and therapies for BrS

As discussed above, the occurrence of P2R is determined by the parameter threshold and the parameter range, and different ionic currents and their different components affect these properties differently. So far 23 BrS mutations have been identified [48] causing either a loss of function of I_{Na} or $I_{Ca,L}$, or a gain of function of I_{to} or I_{K-ATP}. Our simulation results show that P2R is promoted by reduction of I_{Na} (Fig.7) or $I_{Ca,L}$ (Fig.6), or increase of I_{to} (Fig.2) or I_{K-ATP} (Fig.8), agreeing in general with the clinical consequences of the BrS mutations. In addition, our simulations offer the following insights into the genesis and prevention of arrhythmias for BrS:

1. I_{to} amplitude needs to be large enough but not too large for P2R to occur, i.e., there is a range of optimal I_{to} strength for P2R (Fig.2). The P2R region becomes smaller as the late component increases and then completely disappears. Prior to the P2R region (i.e., in "Spike & Dome" region), the ST-segment is coved. Beyond the P2R region (i.e., in the "Spike" region), particularly for large late I_{to}, the ST-segment becomes saddleback. Therefore, to suppress P2R using I_{to} as a target, one can either block the I_{to} amplitude or enhance its late component. However, a drug preferentially blocking the late component may convert a type 2 ECG to a type 1 ECG and promote P2R.

2. As for $I_{Ca,L}$ (Fig.6), when I_{to} is strong, reducing the maximum conductance of $I_{Ca,L}$ promotes P2R, in agreement with the general knowledge of the effects of $I_{Ca,L}$ on P2R and arrhythmogenesis in BrS. Interestingly, blocking the window or the late components of $I_{Ca,L}$ does not promote P2R, but instead suppress P2R, providing a novel therapeutic target for BrS.

3. As for I_{Na} (Fig.7), blocking either the peak or the late component can promote P2R, with the late component being more sensitive. While increasing late I_{Na} can suppress P2R, however, it is well-known that increasing late I_{Na} can also promote long QT associated arrhythmias.

Note that in real hearts, I_{to} is not the only transient outward current. Other transient outward currents can exhibit similar effects as I_{to} to influence the genesis of P2R. For example, the Ca^{2+}-activated small conductance K^+ current is a transient outward current [49, 50] known to promote J-wave syndrome and P2R [51–53]. The Ca^{2+}-activated chloride current is also a spiky transient outward current [54, 55] that may potentiate P2R. On the other hand, the late

components of these currents are likely to have the same effects as those of late I_{to}. These currents may contribute to the ECG morphologies and P2R genesis in the real heart.

Limitations

Several limitations should be mentioned. Pseudo-ECGs were calculated in 2D tissue and a whole-heart simulation may result in more realistic ECG morphologies [56]. We mainly simulated the endo-epi heterogeneity in I_{to} conductance. P2R can occur due to the I_{to} heterogeneities in the epicardium, or due to transmural or base-to-apex heterogeneities of other ionic currents. It also hypothesized that regional slow conduction in the right ventricle due to fibrosis can also result in coved ECG morphology [57], and may provide an alternative or synergistic mechanism promoting reentrant arrhythmias in BrS (the so-called depolarization hypothesis [58]), which is a subject for investigation in future simulation studies.

Conclusions

While the peak I_{to} promotes the type 1 ECG morphology and P2R in BrS, the late component can convert type 1 to type 2 ECG and suppress P2R. The late I_{to} can also stabilize spiral wave reentry, converting VF to VT. Therefore, blocking the peak I_{to} is antiarrhythmic but blocking the late component can be proarrhythmic in patients with BrS. Our simulations also show that blocking either the peak or the late I_{Na} can be proarrhythmic. Blocking the peak $I_{Ca,L}$ is also proarrhythmic, whereas blocking the window or the late $I_{Ca,L}$ components are antiarrhythmic. These observations may provide valuable insights for guiding the development of novel therapeutic targets for prevention of arrhythmias in BrS.

Supplementary Material

Refer to Web version on PubMed Central for supplementary material.

Sources of funding:

Non-standard Abbreviations and Acronyms

1D	1-dimensional
2D	2-dimensional
AP	action potential
APD	action potential duration
BrS	Brugada syndrome
CL	cycle length
DI	diastolic interval

ECG	electrocardiogram
PVC	premature ventricular complex
PCL	pacing cycle length
P2R	phase 2 reentry
VT	ventricular tachycardia
VF	ventricular fibrillation
Na^+	sodium ion
Ca^{2+}	calcium ion
K^+	potassium ion
I_{to}	transient outward potassium current
$I_{Ca,L}$	L-type calcium current
I_{Kr}	rapid component of the delayed rectifier potassium current
I_{Ks}	slow component of the delayed rectifier potassium current
I_{Na}	sodium current
I_{K-ATP}	ATP-sensitive potassium current
I_{NaL}	late sodium current
G_{to}	maximum conductance of I_{to}
P_{Ca}	maximum conductance of $I_{Ca,L}$
G_{Na}	maximum conductance of I_{Na}
G_{NaL}	maximum conductance of I_{NaL}
G_{Kr}	maximum conductance of I_{Kr}
G_{Ks}	maximum conductance of I_{Ks}
G_{K-ATP}	maximum conductance of I_{K-ATP}
γ	parameter controlling strength of late I_{to}

References

1. Brugada P, Brugada J. Right bundle branch block, persistent ST segment elevation and sudden cardiac death: A distinct clinical and electrocardiographic syndrome: A multicenter report. J Am Coll Cardiol. 1992;20:1391–1396. [PubMed: 1309182]

2. Brugada J, Brugada R, Brugada P. Right Bundle-Branch Block and ST-Segment Elevation in Leads V1 Through V3. Circulation. 1998;97:457–460. [PubMed: 9490240]

3. Antzelevitch C, Brugada P, Brugada J, Brugada R, Shimizu W, Gussak I, Riera ARP. Brugada Syndrome. Circ Res. 2002;91:1114–1118. [PubMed: 12480811]

4. Antzelevitch C, Yan G-X. J-wave syndromes: Brugada and early repolarization syndromes. Heart Rhythm. 2015;12:1852–1866. [PubMed: 25869754]

5. Priori SG, Blomström-Lundqvist C, Mazzanti A, Blom N, Borggrefe M, Camm J, Elliott PM, Fitzsimons D, Hatala R, Hindricks G, et al. 2015 ESC Guidelines for the management of patients with ventricular arrhythmias and the prevention of sudden cardiac death: The Task Force for the Management of Patients with Ventricular Arrhythmias and the Prevention of Sudden Cardiac Death of the European Society of Cardiology (ESC)Endorsed by: Association for European Paediatric and Congenital Cardiology (AEPC). Eur Heart J. 2015;36:2793–2867. [PubMed: 26320108]

6. Wilde AAM, Antzelevitch C, Borggrefe M, Brugada J, Brugada R, Brugada P, Corrado D, Hauer RNW, Kass RS, Nademanee K, et al. Proposed Diagnostic Criteria for the Brugada Syndrome. Circulation. 2002;106:2514–2519. [PubMed: 12417552]

7. Antzelevitch C, Yan G-X, Ackerman MJ, Borggrefe M, Corrado D, Guo J, Gussak I, Hasdemir C, Horie M, Huikuri H, et al. J-Wave syndromes expert consensus conference report: Emerging concepts and gaps in knowledge. Heart Rhythm. 2016;13:e295–e324. [PubMed: 27423412]

8. Priori SG, Gasparini M, Napolitano C, Bella PD, Ottonelli AG, Sassone B, Giordano U, Pappone C, Mascioli G, Rossetti G, et al. Risk Stratification in Brugada Syndrome. J Am Coll Cardiol. 2012;59:37–45. [PubMed: 22192666]

9. Antzelevitch C The Brugada syndrome: ionic basis and arrhythmia mechanisms. J Cardiovasc Electrophysiol. 2001;12:268–272. [PubMed: 11232628]

10. Di Diego JM, Antzelevitch C. Pinacidil-induced electrical heterogeneity and extrasystolic activity in canine ventricular tissues. Does activation of ATP-regulated potassium current promote phase 2 reentry? Circulation. 1993;88:1177–1189. [PubMed: 7689041]

11. Lukas A, Antzelevitch C. Phase 2 reentry as a mechanism of initiation of circus movement reentry in canine epicardium exposed to simulated ischemia. Cardiovasc Res. 1996;32:593–603. [PubMed: 8881520]

12. Yan GX, Antzelevitch C. Cellular basis for the Brugada syndrome and other mechanisms of arrhythmogenesis associated with ST-segment elevation. Circulation. 1999;100:1660–1666. [PubMed: 10517739]

13. Luo CH, Rudy Y. A dynamical model of the cardiac ventricular action potential: I. simulations of ionic currents and concentration changes. Circ. Res. 1994;74:1071–1096. [PubMed: 7514509]

14. ten Tusscher KH, Noble D, Noble PJ, Panfilov AV. A model for human ventricular tissue. Am J Physiol Heart Circ Physiol. 2004;286:H1573–1589. [PubMed: 14656705]

15. Dumaine R, Towbin JA, Brugada P, Vatta M, Nesterenko DV, Nesterenko VV, Brugada J, Brugada R, Antzelevitch C. Ionic Mechanisms Responsible for the Electrocardiographic Phenotype of the Brugada Syndrome Are Temperature Dependent. Circ Res. 1999;85:803–809. [PubMed: 10532948]

16. Landaw J, Yuan X, Chen P- S, Qu Z. The transient outward potassium current plays a key role in spiral wave breakup in ventricular tissue. Am J Physiol Heart Circ Physiol. 2021;320:H826–H837. [PubMed: 33385322]

17. Lukas A, Antzelevitch C. Differences in the electrophysiological response of canine ventricular epicardium and endocardium to ischemia. Role of the transient outward current. Circulation. 1993;88:2903–2915. [PubMed: 8252704]

18. Clancy CE, Rudy Y. Na(+) channel mutation that causes both Brugada and long-QT syndrome phenotypes: a simulation study of mechanism. Circulation. 2002;105:1208–1213. [PubMed: 11889015]

19. Hopenfeld B Mechanism for action potential alternans: the interplay between L-type calcium current and transient outward current. Heart Rhythm. 2006;3:345–352. [PubMed: 16500310]

20. Landaw J, Garfinkel A, Weiss JN, Qu Z. Memory-Induced Chaos in Cardiac Excitation. Phys Rev Lett. 2017;118:138101. [PubMed: 28409990]

21. Landaw J, Qu Z. Memory-induced nonlinear dynamics of excitation in cardiac diseases. Phys Rev E. 2018;97:042414. [PubMed: 29758700]

22. Aiba T, Shimizu W, Hidaka I, Uemura K, Noda T, Zheng C, Kamiya A, Inagaki M, Sugimachi M, Sunagawa K. Cellular Basis for Trigger and Maintenance of Ventricular Fibrillation in the Brugada Syndrome Model: High-Resolution Optical Mapping Study. J Am Coll Cardiol. 2006;47:2074–2085. [PubMed: 16697328]

23. Hund TJ, Rudy Y. Rate dependence and regulation of action potential and calcium transient in a canine cardiac ventricular cell model. Circulation. 2004;110:3168–3174. [PubMed: 15505083]

24. Milman A, Gourraud J-B, Andorin A, Postema PG, Sacher F, Mabo P, Conte G, Giustetto C, Sarquella-Brugada G, Hochstadt A, et al. Gender differences in patients with Brugada syndrome and arrhythmic events: Data from a survey on arrhythmic events in 678 patients. Heart Rhythm. 2018;15:1457–1465. [PubMed: 29908370]

25. Yamaki M, Sato N, Okada M, Fujita S, Go K, Sakamoto N, Tanabe Y, Takeuchi T, Kawamura Y, Hasebe N. A Case of Brugada Syndrome in Which Diurnal ECG Changes Were Associated With Circadian Rhythms of Sex Hormones. Int Heart J. 2009;50:669–676. [PubMed: 19809215]

26. Kim S-H, Nam G-B, Baek S, OH Choi H, Hun KIm K, Choi K-J, Joung B, Pak H-N, Lee M-H, Soon Kim S, et al. Circadian and Seasonal Variations of Ventricular Tachyarrhythmias in Patients with Early Repolarization Syndrome and Brugada Syndrome: Analysis of Patients with Implantable Cardioverter Defibrillator. J Cardiovasc Electrophysiol. 2012;23:757–763. [PubMed: 22353358]

27. Takigawa M, Noda T, Shimizu W, Miyamoto K, Okamura H, Satomi K, Suyama K, Aihara N, Kamakura S, Kurita T. Seasonal and circadian distributions of ventricular fibrillation in patients with Brugada syndrome. Heart Rhythm. 2008;5:1523–1527. [PubMed: 18984526]

28. Matsuo K, Kurita T, Inagaki M, Kakishita M, Aihara N, Shimizu W, Taguchi A, Suyama K, Kamakura S, Shimomura K. The circadian pattern of the development of ventricular fibrillation in patients with Brugada syndrome. Eur Heart J. 1999;20:465–470. [PubMed: 10213350]

29. Chen M, Fei Y, Chen T-Z, Li Y-G, Chen P-S. The regulation of the small-conductance calcium-activated potassium current and the mechanisms of sex dimorphism in J wave syndrome. Pflügers Archiv - European Journal of Physiology. 2021;473:491–506. [PubMed: 33411079]

30. Yang P-C, Perissinotti LL, López-Redondo F, Wang Y, DeMarco KR, Jeng M-T, Vorobyov I, Harvey RD, Kurokawa J, Noskov SY, et al. A multiscale computational modelling approach predicts mechanisms of female sex risk in the setting of arousal-induced arrhythmias. J Physiol. 2017;595:4695–4723. [PubMed: 28516454]

31. Kurokawa J, Kodama M, Clancy CE, Furukawa T. Sex hormonal regulation of cardiac ion channels in drug-induced QT syndromes. Pharmacol Ther. 2016;168:23–28. [PubMed: 27595633]

32. Odening KE, Koren G. How do sex hormones modify arrhythmogenesis in long QT syndrome? Sex hormone effects on arrhythmogenic substrate and triggered activity. Heart Rhythm. 2014;11:2107–2115. [PubMed: 24954242]

33. Gaborit N, Varro A, Le Bouter S, Szuts V, Escande D, Nattel S, Demolombe S. Gender-related differences in ion-channel and transporter subunit expression in non-diseased human hearts. J Mol Cell Cardiol. 2010;49:639–646. [PubMed: 20600101]

34. Sims C, Reisenweber S, Viswanathan PC, Choi BR, Walker WH, Salama G. Sex, age, and regional differences in L-type calcium current are important determinants of arrhythmia phenotype in rabbit hearts with drug-induced long QT type 2. Circ Res. 2008;102:e86–100. [PubMed: 18436794]

35. Pennartz CMA, de Jeu MTG, Bos NPA, Schaap J, Geurtsen AMS. Diurnal modulation of pacemaker potentials and calcium current in the mammalian circadian clock. Nature. 2002;416:286–290. [PubMed: 11875398]

36. Chen Y, Zhu D, Yuan J, Han Z, Wang Y, Qian Z, Hou X, Wu T, Zou J. CLOCK-BMAL1 regulate the cardiac L-type calcium channel subunit CACNA1C through PI3K-Akt signaling pathway. Can J Physiol Pharmacol. 2016;94:1023–1032. [PubMed: 27376484]

37. Jeyaraj D, Haldar SM, Wan X, McCauley MD, Ripperger JA, Hu K, Lu Y, Eapen BL, Sharma N, Ficker E, et al. Circadian rhythms govern cardiac repolarization and arrhythmogenesis. Nature. 2012;483:96–99. [PubMed: 22367544]

38. Shaw RM, Rudy Y. Electrophysiologic effects of acute myocardial ischemia: a theoretical study of altered cell excitability and action potential duration. Cardiovasc Res. 1997;35:256–272. [PubMed: 9349389]

39. Qu Z, Weiss JN. Mechanisms of Ventricular Arrhythmias: From Molecular Fluctuations to Electrical Turbulence. Annu Rev Physiol. 2015;77:29–55. [PubMed: 25340965]

40. Maoz A, Krogh-Madsen T, Christini DJ. Instability in action potential morphology underlies phase 2 reentry: a mathematical modeling study. Heart Rhythm. 2009;6:813–822. [PubMed: 19467510]

41. Miyoshi S, Mitamura H, Fujikura K, Fukuda Y, Tanimoto K, Hagiwara Y, Ita M, Ogawa S. A mathematical model of phase 2 reentry: role of L-type Ca current. Am J Physiol Heart Circ Physiol. 2003;284:H1285–1294. [PubMed: 12531737]

42. Zhang Z, Qu Z. Life and death saddles in the heart. Phys Rev E. 2021;103:062406. [PubMed: 34271754]

43. Li G-R, Wang H-B, Qin G-W, Jin M-W, Tang Q, Sun H-Y, Du X-L, Deng X-L, Zhang X-H, Chen J-B, et al. Acacetin, a Natural Flavone, Selectively Inhibits Human Atrial Repolarization Potassium Currents and Prevents Atrial Fibrillation in Dogs. Circulation. 2008;117:2449–2457. [PubMed: 18458165]

44. Di Diego JM, Patocskai B, Barajas-Martinez H, Borbáth V, Ackerman MJ, Burashnikov A, Clatot J, Li G-R, Robinson VM, Hu D, et al. Acacetin suppresses the electrocardiographic and arrhythmic manifestations of the J wave syndromes. PLOS ONE. 2020;15:e0242747. [PubMed: 33232375]

45. Yamashita T, Nakajima T, Hamada E, Hazama H, Omata M, Kurachi Y. Flecainide inhibits the transient outward current in atrial myocytes isolated from the rabbit heart. The Journal of pharmacology and experimental therapeutics. 1995;274:315–321. [PubMed: 7616415]

46. Wang Z, Fermini B, Nattel S. Effects of flecainide, quinidine, and 4-aminopyridine on transient outward and ultrarapid delayed rectifier currents in human atrial myocytes. The Journal of pharmacology and experimental therapeutics. 1995;272:184–196. [PubMed: 7815332]

47. Bébarová M, Matejovic P, Pásek M, Simurdová M, Simurda J. Effect of ajmaline on transient outward current in rat ventricular myocytes. General physiology and biophysics. 2005;24:27–45. [PubMed: 15900085]

48. Antzelevitch C, Di Diego JM. J wave syndromes: What's new? Trends Cardiovasc Med. 2021;(in press)

49. Hamilton S, Polina I, Terentyeva R, Bronk P, Kim TY, Roder K, Clements RT, Koren G, Choi B-R, Terentyev D. PKA phosphorylation underlies functional recruitment of sarcolemmal SK2 channels in ventricular myocytes from hypertrophic hearts. J Physiol. 2020;598:2847–2873. [PubMed: 30771223]

50. Terentyev D, Rochira JA, Terentyeva R, Roder K, Koren G, Li W. Sarcoplasmic reticulum Ca2+ release is both necessary and sufficient for SK channel activation in ventricular myocytes. Am J Physiol Heart Circ Physiol. 2014;306:H738–H746. [PubMed: 24381116]

51. Chen M, Xu D-Z, Wu AZ, Guo S, Wan J, Yin D, Lin S-F, Chen Z, Rubart-von der Lohe M, Everett THIV, et al. Concomitant SK current activation and sodium current inhibition cause J wave syndrome. JCI Insight. 2018;3:e122329.

52. Landaw J, Zhang Z, Song Z, Liu MB, Olcese R, Chen P-S, Weiss JN, Qu Z. Small-conductance Ca2+-activated K+ channels promote J-wave syndrome and phase 2 reentry. Heart Rhythm. 2020;17:1582–1590. [PubMed: 32333974]

53. Fei Y-D, Chen M, Guo S, Ueoka A, Chen Z, Rubart-von der Lohe M, Everett TH, Qu Z, Weiss JN, Chen P-S. Simultaneous activation of the small conductance calcium-activated potassium current by acetylcholine and inhibition of sodium current by ajmaline cause J-wave syndrome in Langendorff-perfused rabbit ventricles. Heart Rhythm. 2021;18:98–108. [PubMed: 32763429]

54. Hegyi B, Bossuyt J, Griffiths LG, Shimkunas R, Coulibaly Z, Jian Z, Grimsrud KN, Sondergaard CS, Ginsburg KS, Chiamvimonvat N, et al. Complex electrophysiological remodeling in postinfarction ischemic heart failure. Proc Natl Acad Sci USA. 2018;115:E3036–E3044. [PubMed: 29531045]

55. Verkerk AO, Veldkamp MW, Baartscheer A, Schumacher CA, Klöpping C, Ginneken ACGv, Ravesloot JH. Ionic Mechanism of Delayed Afterdepolarizations in Ventricular Cells Isolated From Human End-Stage Failing Hearts. Circulation. 2001;104:2728–2733. [PubMed: 11723027]

56. Xia L, Zhang Y, Zhang H, Wei Q, Liu F, Crozier S. Simulation of Brugada syndrome using cellular and three-dimensional whole-heart modeling approaches. Physiol Meas. 2006;27:1125–1142. [PubMed: 17028406]

57. Hoogendijk MG, Opthof T, Postema PG, Wilde AAM, de Bakker JMT, Coronel R. The Brugada ECG Pattern. Circ Arrhythm Electrophysiol. 2010;3:283–290. [PubMed: 20551422]

58. Weiss JN. Arrhythmias in Brugada syndrome: Defective depolarization, repolarization or both? JACC Clin Electrophysiol. 2021;7:271–272. [PubMed: 33602411]

What is known?

- Three types of characteristic ECGs are associated with Brugada syndrome, only type 1 (coved ST-segment) is diagnostic.

- Phase 2 reentry induced by Ito is a candidate mechanism of arrhythmias in Brugada syndrome.

What the study adds?

- Computer simulations provide mechanistic insights into why only type 1 is diagnostic, showing that the peak Ito promotes type 1 ECG and phase 2 reentry, but the late component of Ito converts coved ECG into saddleback (type 2) ECG and suppresses phase 2 reentry.

- Besides the well-known fact that blocking an inward current or enhancing an outward current promotes phase 2 reentry, blocking the window and late calcium current suppresses phase 2 reentry.
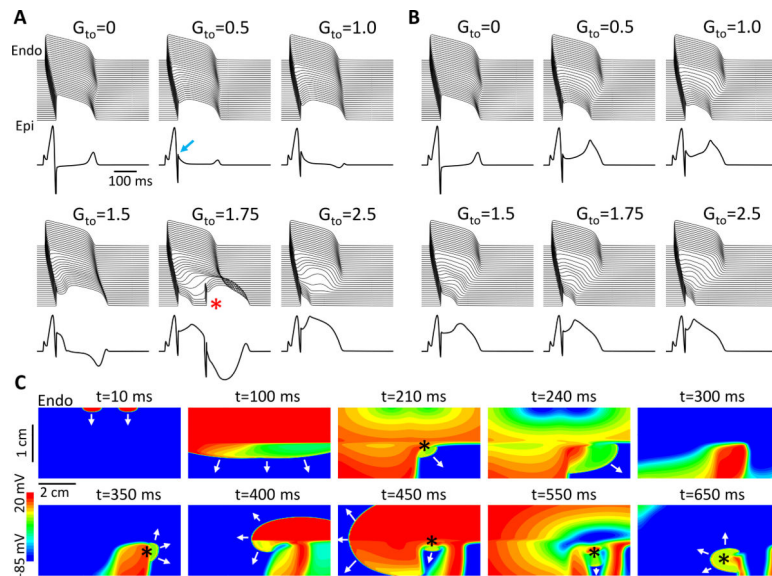
Figure 1. Effects of late I_{to} on ST-segment properties and P2R.

Simulations were carried out in a 2D tissue model with an endocardial-to-epicardial I_{to} gradient. **A**. Time-space plots of V and ECGs for different levels of G_{to} (in unit mS/cm^2) when $\gamma = 0$. The arrow in the 2nd panel points to the elevated J-point. The asterisk in the 5th panel indicates the P2R/PVC. **B**. Same as A but when $\gamma = 0.1$. **C**. Wave dynamics in the same 2D tissue as for A but with an I_{to} heterogeneity in the longitudinal direction. Shown are voltage snapshots at different time points. Arrows indicate propagating wavefronts. A wave elicited from two stimulus sites (t=10 ms) propagated from the endocardium to epicardium (t=100 ms). Due to the early repolarization in the lower-right quadrant, a P2R occurred (t=210 ms, marked by *), propagated toward the tissue boundary (t=240 ms) and disappeared. The repolarization pattern remained heterogeneous (t=300 ms) and a new P2R occurred (t=350 ms) that propagated as a spiral wave reentry (t=400 ms) before wandering off the tissue boundary (t=450 ms). New P2Rs (*) also occurred in snapshots at t=450, 550, and 650 ms. Due to the tissue size, the last P2R shown in t=650 ms was not able to survive, and the tissue became quiescent before the next pacing beat. See Movie I in Data Supplement for the detailed wave dynamics. Tissue size was 7.68 cm $\times$ 1.92 cm.
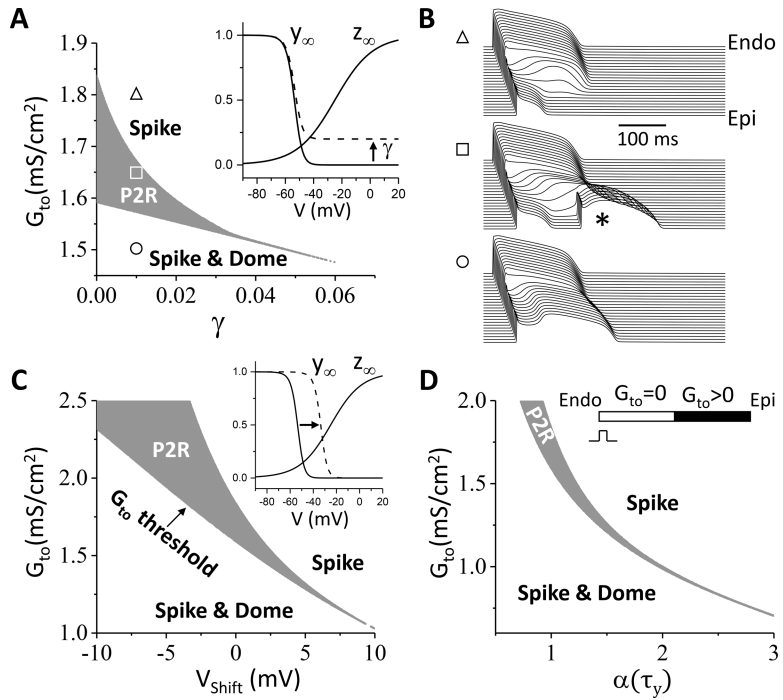
Figure 2. Effects of I_{to} properties on P2R.
1D cable simulations with a single pacing beat from the endocardium. The cable is uniform except that I_{to} is heterogeneous as indicated in the inset of panel D. The gray region is the P2R region. The region marked by "Spike & Dome" is the region where the AP is normal or exhibits a spike-and-dome morphology in the endocardial side (see the lower panel in B). The region marked by "Spike" is the region where the AP in the epicardial side becomes a spike with a very abbreviated APD (see the upper panel in B). The boundary between the "Spike & Dome" region to the "P2R" region is the threshold for P2R as indicated in C. **A**. P2R region versus G_{to} and γ. γ (Eq.4) controls the level of incomplete inactivation of the steady state as indicated in the inset. **B**. Space and time plots of V from the parameter locations marked in A. Asterisk indicates the PVC. **C**. P2R region versus G_{to} and the voltage shift (V_{shift}) of the steady-state inactivation curve (y_∞) as indicated in the inset. $V_{shift} > 0$ means a right shift and vice versa. **D**. P2R region versus G_{to} and the inactivation time constant τ_y. α (τ_y) is the fold change of τ_y.
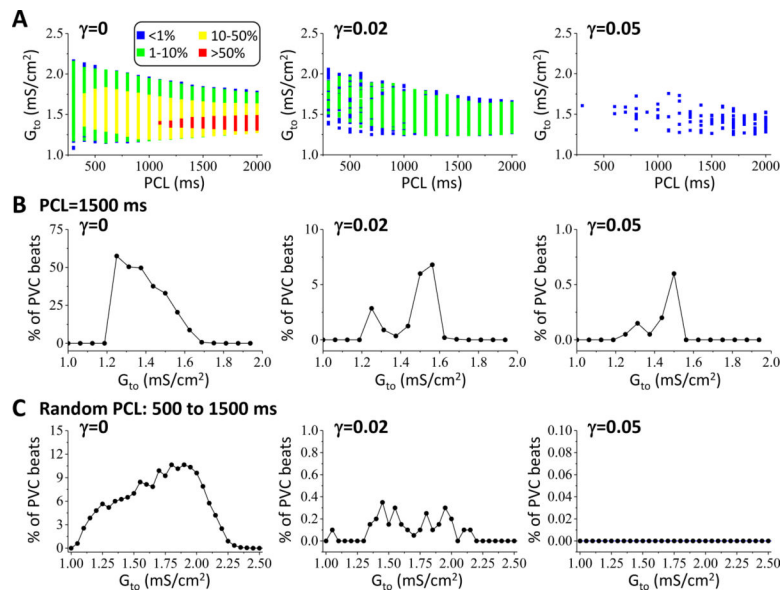
Figure 3. Dependence of P2R on heart rate and late I_{to}.
1D cable simulations with periodic or random pacing from the endocardium. **A**. Percentage of beats exhibiting PVCs versus G_{to} and PCL under periodic pacing for $\gamma = 0$, $\gamma = 0.02$, and $\gamma = 0.05$. 200 pacing beats were applied for each combination of G_{to} and PCL. Color scale indicates the percentage of PVC beats. **B**. Histograms showing percentage of PVC beats versus G_{to} for $\gamma = 0$, $\gamma = 0.02$, and $\gamma = 0.05$ under periodic pacing with PCL=1500 ms. 2000 pacing beats were applied for each G_{to}. **C**. Same as B but for the random pacing protocol with random PCLs uniformly drawn from the interval between 500 ms and 1500 ms.
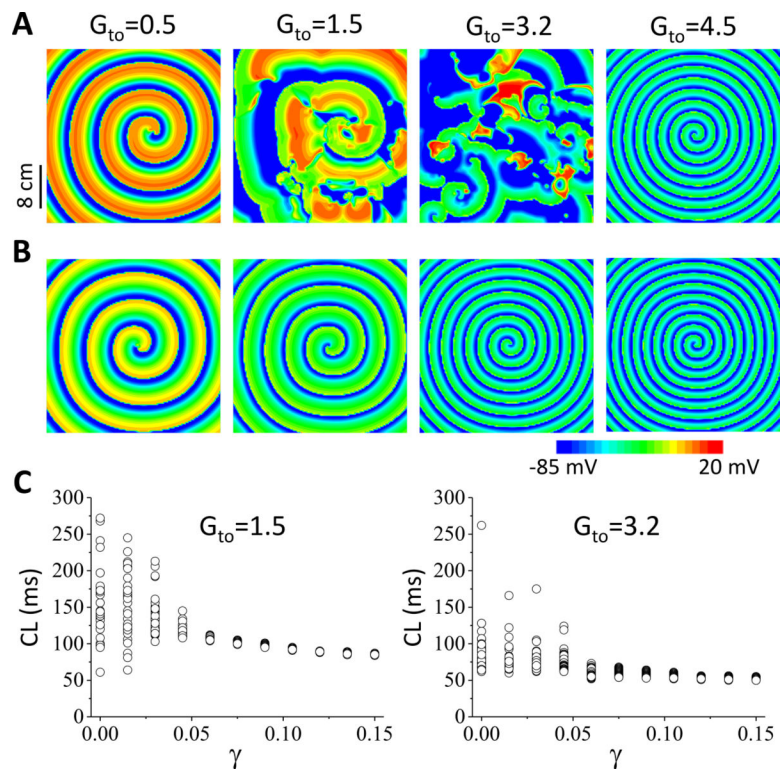
Figure 4. Effects of late I_{to} on reentry stability in 2D homogeneous tissue.
A. Voltage snapshots for different G_{to} (in unit mS/cm^2) for $\gamma = 0$. **B**. Same as A but for $\gamma = 0.15$. **C**. Cycle length (CL) of reentry versus γ for G_{to}=1.5 mS/cm^2 and 3.2 mS/cm^2. Since the tissue is homogeneous, reentry cannot occur spontaneous, and thus it was induced using the traditional cross-field protocol.
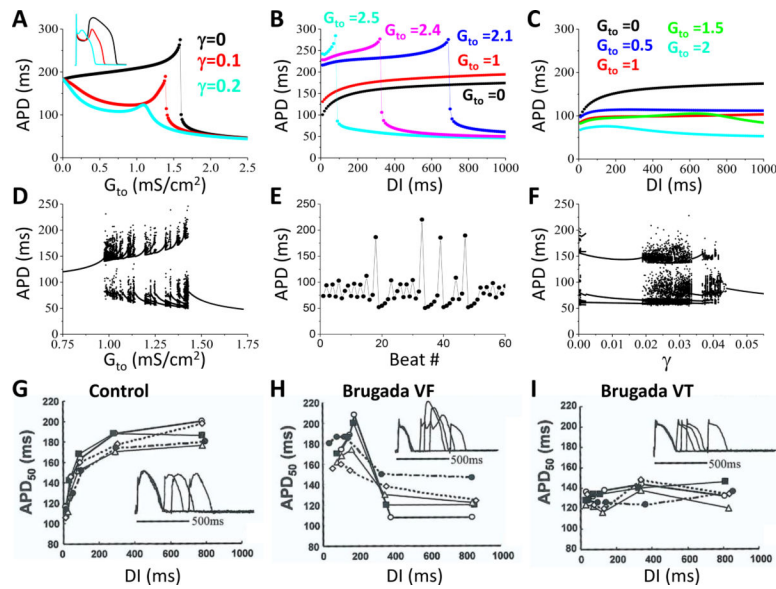
Figure 5. Effects of late I_{to} on cellular properties.

A. APD versus G_{to} for three different γ values as marked. Inset shows the APs from the peaks of the three curves. **B**. S1S2 APD restitution for $\gamma = 0$ and different G_{to} as marked. **C**. S1S2 APD restitution for $\gamma = 0.2$ and different G_{to} as marked. **D**. APD versus G_{to} for $\gamma = 0$ under periodic pacing with PCL=500 ms. 200 consecutive APDs are plotted for each G_{to}. **E**. APD versus beat # for $G_{to}=1.425$ mS/cm^2 from a simulation in D. **F**. APD versus γ for $G_{to}=1.25$ mS/cm^2 under periodic pacing with PCL=500 ms. **G-I**. S1S2 APD restitution curves measured in experiments by Aiba et al [22] for control (G), the ones exhibiting VF (H), and the ones exhibiting VT (I). Panels G-I were modified from Aiba et al with permission.
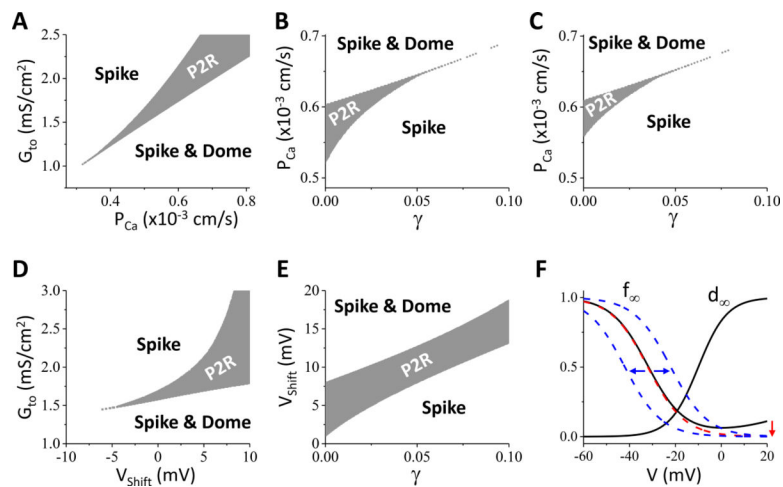
Figure 6. Effects of I$_{Ca,L}$ on P2R.
Simulations were carried out in a 1D cable as for Fig.2. **A**. P2R versus P$_{Ca}$ and G$_{to}$ for γ = 0. P$_{Ca}$ is a parameter proportional to the maximum conductance of I$_{Ca,L}$. **B**. P2R region versus γ and P$_{Ca}$ for G$_{to}$=1.75 mS/cm^2. **C**. Same as B but after removing the late component of I$_{Ca,L}$. This was done by removing the elevated part of the original f_∞ in the high voltage range as indicated in panel F. **D**. Effects of window I$_{Ca,L}$ on P2R, simulated by shifting f_∞ as indicated in panel F. Shown is the P2R region versus V$_{shift}$ and G$_{to}$. **E**. P2R region versus γ and V$_{shift}$. G$_{to}$=1.75 mS/cm^2. **F**. Alterations of f_∞. Solid black curve is the original f_∞. Dashed red curve is the one after the late component removed, corresponding the change from panel B to panel C. Dashed blue curves indicate the right or left shift from the dashed red curve used in D and E. V$_{shift}$>0 for the right shift and V$_{shift}$<0 for the left shift.
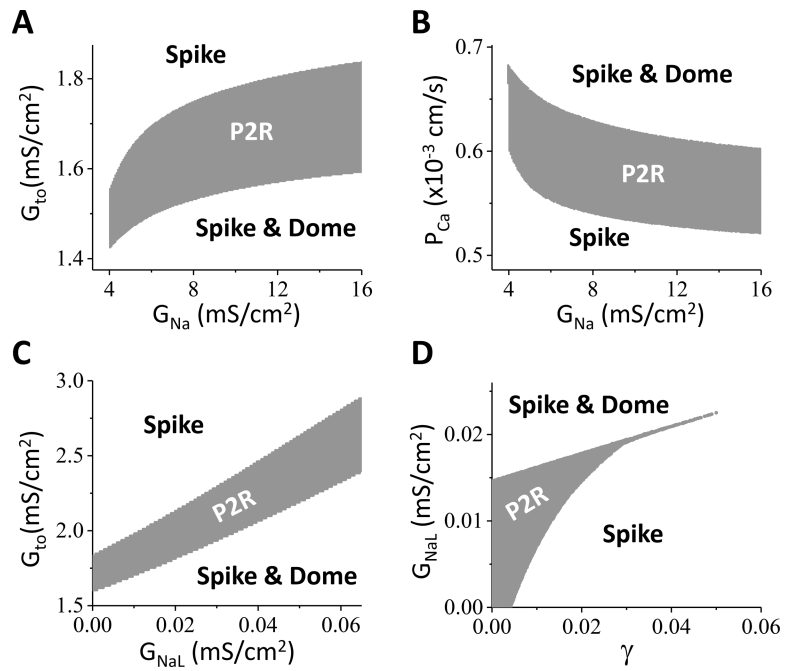
Figure 7. Effects of I_{Na} on P2R.

Simulations were carried out in a 1D cable as for Fig.2. **A**. P2R region versus G_{Na} and G_{to}. **B**. P2R region versus G_{Na} and P_{Ca}. $G_{to}=1.75$ mS/cm². **C**. P2R region versus G_{NaL} and G_{to}. **D**. P2R region versus γ and G_{NaL}. In A and B, $G_{NaL}=0$.
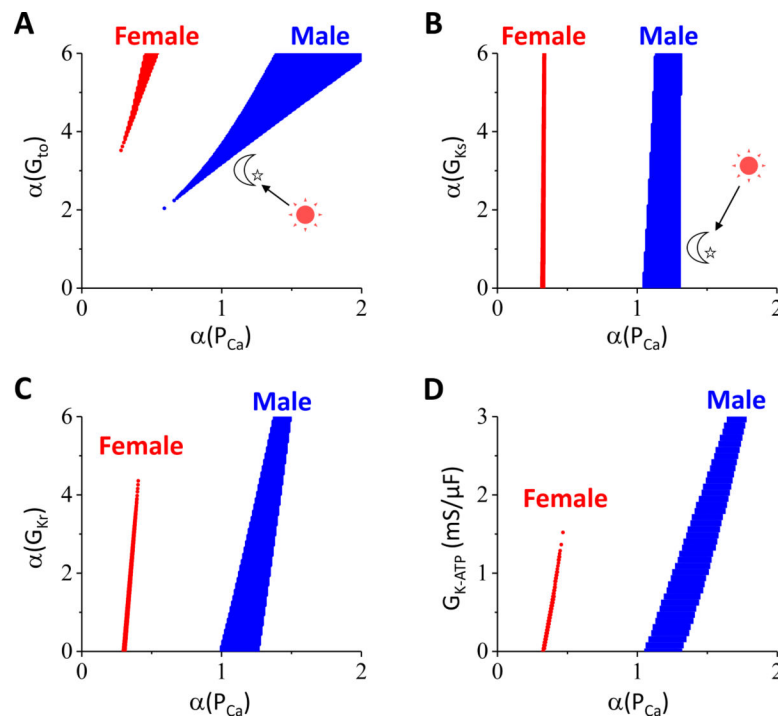
Figure 8. Effects of sex difference and circadian rhythm on P2R.
Simulations were done in the 1D cable as for Fig.2 except that the maximum conductances of ionic currents were different for female and male. The control parameters for male were the same as for Fig.2. The female-to-male ratios of the maximum conductance were shown in Table I in Data Supplement. α is the fold change of the maximum conductance from the control values. For example, $\alpha(P_{Ca})$ implies the P_{Ca} value is α-fold of the control P_{Ca} for either female or male. Similar to Fig.6A, the "Spike & Dome" region is in the right and the "Spike" region is in left of the P2R region for all the panels in this figure. **A**. P2R regions for male and female versus $\alpha(P_{Ca})$ and $\alpha(G_{to})$. **B**. P2R regions for male and female versus $\alpha(P_{Ca})$ and $\alpha(G_{Ks})$. **C**. P2R regions for male and female versus $\alpha(P_{Ca})$ and $\alpha(G_{Kr})$. **D**. P2R regions for male and female versus $\alpha(P_{Ca})$ and G_{K-ATP}. Since there was no I_{K-ATP} in control, G_{K-ATP} instead of $\alpha(G_{K-ATP})$ was used in this panel. $\alpha(G_{to})$=4 was used for B-D. Note that the P2R region in D is more tilted to the right than those in B and C, indicating that I_{K-ATP} exhibits a larger effect in changing the $I_{Ca,L}$ threshold for P2R and thus a larger effect on promoting P2R. In the ten Tusscher human model, we observed an even more tilted P2R region which also expanded as G_{K-ATP} increased (see Fig.XD in Data Supplement).